J Appl Electrochem (2014) 44:995–1006
DOI 10.1007/s10800-014-0720-0

RESEARCH ARTICLE

Hydrodynamic analysis of flow fields for redox flow battery applications

T. Jyothi Latha · S. Jayanti

Received: 24 April 2014 / Accepted: 14 July 2014 / Published online: 17 August 2014

Abstract Electrolyte flow distribution is an important factor that contributes to the performance of the overall efficiency of a redox flow battery system. In the present paper, a comparative study of the hydrodynamics of the serpentine and interdigitated flow fields has been performed. Ex situ experiments were conducted using the two flow fields in conditions typical of flow battery applications. Limited in situ testing has also been conducted. These bring out the surprising result that the pressure drop in the interdigitated flow field is less than that in the serpentine for the same flow rate. Computational fluid dynamics studies show strong under-the-rib convection in the reaction zone exists in both flow fields but with a shorter residence time in case of the interdigitated. It is posited that this may explain the superior electrochemical performance of cells with interdigitated flow fields.

Keywords Redox flow battery · Electrolyte · Flow field · Pressure drop · Efficiency

1 Introduction

The need and demand for large-scale energy storage have been increasing especially with anticipated problems of grid instability arising from expanding solar and wind integration with the conventional electricity grid. With the conventional integrated-cell based battery systems, increasing the ratio of energy to power capacity raises costs markedly and entails more complex engineering that can adversely impact the reliability as well as the safety [1]. Redox flow batteries (RFB) are considered a promising candidate for load leveling/peak shaving [2], being capable of storing a large quantity of electricity for medium to large scale applications in a relatively simple and straightforward design [3, 4]. The all-vanadium redox flow battery (VRFB) is one among such systems. It exhibits several desirable characteristics associated with an electrical energy storage system; these include good electrochemical reversibility, large storage capacity (multi-MWh/MW), deep discharge, high round-trip efficiency, active thermal management, and long cycle life. Despite the excellent performance achieved with the VRFBs, their wide-spread adoption by the global energy sector has been thwarted by economic factors such as high capital cost due to expensive materials such as vanadium and the ion exchange membrane and low electrolyte energy density. However, recent issues with NaS, Li-ion, and lead-acid battery installations, as well as the high cost of Li-ion, have shifted the focus to the VRFB as a favored battery storage technology [5, 6].

A VRFB employs $VO^{2+}/VO_2{}^{+}$ as positive electrolyte and V^{+2}/V^{+3} as negative electrolyte. Both the fluids are stored in external tanks and are pumped through the cell or stack of cells. The electrochemical reactions take place at the porous carbon felt electrodes which are separated by an ion exchange membrane. A vanadium battery system is composed of a cell stack, anolyte, and catholyte tanks with piping connecting the stack and the tanks and the electrolyte pumps. Much of the recent research on vanadium batteries has focused on materials including novel electrode materials to enhance kinetic reversibility on the positive side and new catalysts on different substrates to offset charge imbalance due to hydrogen evolution on the negative side so as to enhance battery performance/efficiency [7–12]; novel/enhanced electrolytes to increase

T. Jyothi Latha · S. Jayanti (✉)
Department of Chemical Engineering, Indian Institute of Technology Madras, Chennai 600036, India
e-mail: sjayanti@iitm.ac.in

energy density and operating temperature range using additives and mixed acid supporting electrolyte [13, 14]; and new ion exchange membranes and separators [15, 16] to replace the conventional and expensive Nafion membrane while ensuring good electrochemical performance with good energy efficiency (>80 %), rate capability, temperature tolerance, exceptional capacity retention capability, and proven chemical stability in the mixed acid VRB system. With increasing electrochemical performance of the batteries, the parasitic power loss from the pumping of the electrolytes becomes important. Pressure drop losses are associated with the system due to the need for continuous circulation of the electrolytes through the cell and are directly dependent on the flow rate as well as on various cell dimensions. Pressure drop losses both in the stack and in the associated pipes between the stack and storage tanks are required to be kept minimum so as to minimize pumping power [17]. At the same time, it is necessary to maintain good supply of fresh electrolyte to the reaction sites. In an RFB, this is achieved by ensuring good cross-flow through the electrode material. A number of flow field designs have been proposed for fuel cell applications [18, 19]. However, as pointed out previously [20], there are fundamental differences between fuel cells and flow batteries which necessitate a fresh look at the flow field design for RFB applications. These differences are in the form of an order of magnitude or higher difference in such fundamental transport parameters as diffusivity of the fluids, permeability of the electrode material, and thickness of the diffusion layer. One can therefore expect significant differences in the cross-flow pattern that is common in serpentine and other flow fields [19, 21].

While a large variety of flow fields can be found for fuel cell applications, four principal patterns are often used in RFB applications; these are the conventional flow field (Fig. 1a), the parallel flow field (Fig. 1b), the serpentine flow field (Fig. 1c), and the interdigitated flow field (Fig. 1d). Flow fields differ in terms of their ability to transport electrolyte to the reaction site and the pressure drop that is required to circulate the electrolyte at a given rate. In the conventional flow field, the electrolyte is introduced directly into the carbon felt electrode at one corners of the cell, and is allowed to distribute itself throughout and flow out from the corner opposite to the inlet port. This leads to high pressure drop as the entire flow has to flow through the porous medium, and maldistribution of the electrolyte is also possible [18, 20] with deleterious consequences on the performance of the cell. Uniform distribution of electrolyte on the electrode surface is needed to minimize mass transfer polarization over the entire electrode. Uniformity can be achieved using higher electrolyte flow rate which enhances VRFB performance in terms of capacity but it also increases pumping power consumption which reduces system efficiency. Therefore, it is required to operate at optimum electrolyte flow rate determined for balanced system efficiency and capacity [22]. A parallel flow field offers the least pressure drop, but severe flow non-uniformity can be expected among the channels [23, 24]. In addition, under-the-rib convection may be negligible and very little convective mass transfer is effected in the porous medium [19, 21].

A number of ex situ and in situ studies of flow field designs have been reported in the literature on redox flow batteries. Hoberecht [17] proposed a conventional flow field with inlet and outlet manifolds so that the fluid can spread out evenly before moving upward through the electrode. He studied the influence of cell geometry and design parameters such as cavity thickness, inlet and outlet flow port width, and depth and flow rate on pressure drop. He found that the compression of the porous electrode is a major contributing factor and accounts for nearly half of the pressure drop. Miyabayashi et al. [25] proposed a cell design with multiple slits in inlet and outlet manifolds to provide a uniform flow distribution pattern and reduce pressure drop. Inoue et al. [26] proposed a porous electrode with convex, semi-circle, and v-shaped grooves. Harper et al. [27] proposed a flow channel design on the bipolar plate to reduce pressure drop and to obtain uniformly distributed flow pattern. In a later work, they proposed an interdigitated channel design for the flow cell [28]. They claimed that the interdigitated channel design could enhance the cell performance without increasing the pressure drop significantly as the electrolyte would flow through the porous electrode. Tian et al. [29] studied numerically various flow designs with single flow inlet and outlet, multiple inlet and outlet, wide single inlet and outlet, wide single inlet and outlet with branched/staggered interdigitated hollow channels in the porous electrode. They concluded that unlike conventional design, the introduction of flow distribution channels would produce better flow uniformity through the electrode, and introduction of channels inside the porous electrode would reduce pressure drop with insignificant net power output loss.

In situ studies of flow fields and flow distribution effects in vanadium redox flow batteries have also been reported. Chen et al. [30] carried out experimental and numerical investigations of electrolyte flow distribution using a parallel flow field for a VRFB. Their results showed a highly non-uniform distribution of the electrolyte over the entire surface with concentrated distribution in the central area of flow field and a vortex flow in the inlet and the outlet regions. Simulated results which fit well with experimental data suggested that an optimized inner flow field structure should be designed. Xu et al. [31] carried out a study on serpentine and parallel flow fields along with conventional

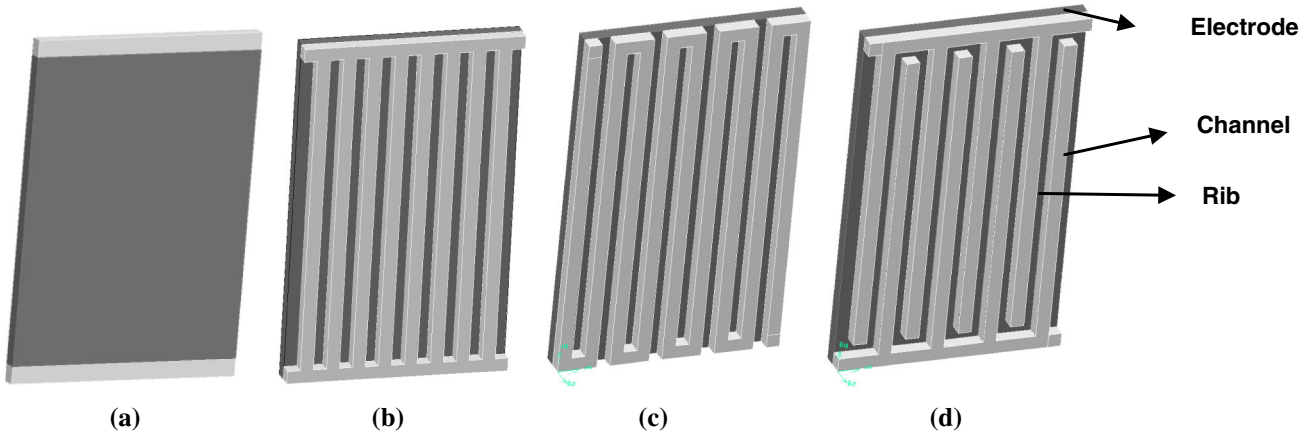

Fig. 1 Schematic representation of flow fields with porous layer **a** without flow field, **b** parallel, **c** serpentine, **d** Interdigitated

configuration using a three-dimensional numerical model. At optimal flow rate, energy based efficiency and round-trip efficiency with a serpentine flow field were found to be the higher and the serpentine flow field was therefore recommended over the other. Zhu et al. [32] investigated experimentally the effects of flow fields with flow through and flow pass patterns. Aaron et al. [33] proposed zero gap cell architecture with serpentine flow field which showed significantly higher power density than the conventional cell structure. Tsushima et al. [34] studied the influence of cell geometry and operating parameters on the performance of a redox flow battery system with serpentine and interdigitated flow fields. They observed better performance with an interdigitated flow field in VRFB than with the serpentine flow field. Koeppel et al. [35] redesigned a VRFB for reduced pressure loss using an interdigitated flow field. Recent theoretical studies describe and account for all the relevant phenomena. A 3D pore scale model based on XCT reconstructed geometry of real carbon felt electrode material has been developed by Qiu et al. [36] to solve for the coupled fluid, species, and charge transport along with the electrochemistry of VRFB. Escudero-González and López-Jiménez [37] introduced a methodology comprising three performance indicators using CFD simulations that determine the flow distribution in a particular geometry of a redox cell.

Thus, a number of studies of flow field designs have been reported for redox flow batteries, and the flow fields are shown to influence the electrochemistry of the cell as well as the energy consumption and round-trip efficiency. Serpentine and interdigitated flow fields have been shown to be superior to the conventional and the parallel type of flow fields. The advantages of the first two appear to stem from the significant and uniform cross-flow or under-the-rib convection that is inherently present in these flow fields. While these have been studied well in the fuel cell context (see for example, [21, 38, 39]), the results appear to be somewhat different for redox flow battery applications. Specifically, while interdigitated flow fields have not found favor in fuel cell applications presumably due to the much higher pressure drop compared to the serpentine flow field [18, 38, 39], they appear to be the flow field of choice for RFBs. In order to resolve this anomaly, an in-depth, experimental and numerical investigation of the hydrodynamics of serpentine and interdigitated flow fields in conditions typically encountered in RFB applications have been carried out as part of the present study. Experiments have been conducted to determine the pressure drop characteristics of three sets of serpentine and interdigitated flow fields in conditions applicable to the RFBs. CFD analysis of the flow field characteristics has been carried out to gain further insight into their behavior. Limited in situ testing in a single-cell VRFB has also been conducted. Details of the studies and the results obtained are discussed below.

2 Experimental studies

2.1 Details of the experiments

A single half cell of length 80 mm and width 51 mm in a flow battery set-up was simulated experimentally using Perspex plates. The experimental set-up was similar to the one used in a previous study [20]; the flow field and the geometrical parameters are different in the present study. One plain plate and a grooved plate with a flow field design were used as the bottom and the top plates, respectively. Two layers of porous carbon felt electrode of thickness 2.5 mm and length and width of 80 × 51 mm were placed between the Perspex plates with a compressible silicone gasket of thickness 3 mm around it. The whole assembly was pressed tightly using bolts and nuts to prevent leakage.

Table 1 Geometrical parameters of flow fields

Design	Cell dimensions length × width (mm)	No. of bends/ channels	Total channel length (mm)	Rib width (mm)
Serpentine	80 × 51	8	936	3
	80 × 43	8	736	2
	80 × 51	12	1052	1
Interdigitated	80 × 51	8	71	3
	80 × 43	9	71	2
	80 × 51	11	72	1

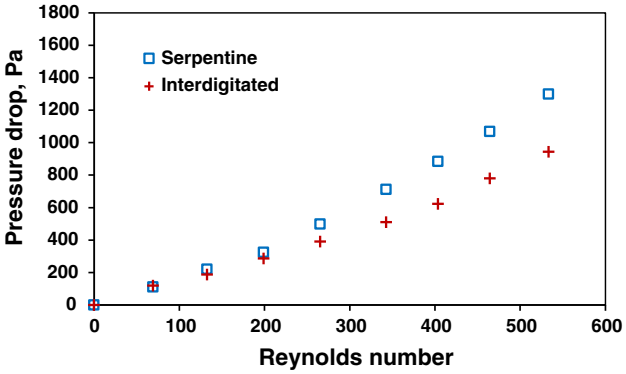

Fig. 2 Comparison of serpentine and interdigitated flow fields of dimensions 80 × 51 mm with rib width of 3 mm

The extent of compression of the silicone gasket/carbon felt was monitored by measuring the gap between the Perspex plates before and after the tightening of the bolts. Water was used as the working fluid and was pumped to the flow frame assembly using a peristaltic pump (Ravel RH-P120S). At a measured flow rate, as the pumped fluid flowed through the channels, the pressure drop between the inlet and the outlet was measured using a U tube manometer. The inlet and the outlet tubes were located normal to the plane of the porous medium. A serpentine flow field of 8 bends with channel cross-section 3 × 3 mm and rib width 3 mm was used as the reference case. In order to bring out of the effect of cross-flow, experiments were conducted with two other serpentine flow fields, each having a rib width of 2 and 1 mm. Comparative experiments were also been carried out with three interdigitated flow fields, with rib widths of 3, 2, and 1 mm. The geometrical details of the six flow fields used in the present study are summarized in Table 1. In all cases, the pressure drop between the inlet and the outlet was measured over the operating flow rate range of 0–122 ml/min giving a Reynolds number (defined based on the inlet channel dimension and the mean flow velocity) range of 0 to about 600. Each set of experiments was repeated thrice to ensure reproducibility. In the absence of special effects such as those associated with two-phase flow, surface wetting characteristics or Knudsen effects associated with microchannels, it is expected that the conclusions on the relative goodness of the flow field drawn from water flow studies would be applicable even for the electrolytes used in VRFB systems.

2.2 Experimental results

The pressure drop in serpentine and interdigitated flow fields was measured over the same inlet liquid flow rate range and is compared in Fig. 2. The surprising result here is that the overall pressure drop for the two is nearly the same for a given inlet flow rate. This is unlike the case of fuel cells where interdigitated flow fields have a much higher pressure drop [18, 19]. This can be attributed primarily to two factors: the significantly lower thickness of the porous (gas diffusion) layer (which translates to a much higher fluid velocity for the same volumetric flow rate) and the much lower permeability of the porous medium in the fuel cells. This implies that the pressure drop required to pump a given liquid flow rate over the same active cell area is slightly less for an interdigitated flow than for a serpentine flow field in redox flow battery systems.

Another important factor in the flow fields is the rib width. A higher rib width will increase the pressure drop in interdigitated flow fields and would lead to lesser under-the-rib convection in serpentine flow fields, which may also have a bearing on the pressure drop. In order to investigate this effect, experiments were carried out in flow fields of roughly similar overall geometries (see Table 1) for rib widths of 3, 2, and 1 mm, while keeping the channel cross-section to be 3 × 3 mm in all cases. In the case of serpentine flow fields, the number of bends was kept the same for rib widths of 2 and 3 mm (with a resulting decrease of 21 % in the overall length and a decrease of 15 % in the active cell area for the former) while it was increased from 8 bends to 12 in the 1 mm rib width case to maintain nearly the same overall cross-sectional area as in the 3 mm case. This led to about 12 % increase in the overall length of the channel, but the overall cell active area was kept the same. In the case of the interdigitated flow field, the number of parallel channels was increased from 8 to 9 and 11 for the 2 and 1 mm rib width cases, respectively. The traversed length of the flow path remained more or less constant while there was a 15 % decrease in the active cell area for the 2 mm rib width case and none in the 1 mm rib width case. The measured pressure drops for these different rib width cases are shown in Figs. 3 and 4 for the serpentine and the interdigitated flow fields, respectively. In each case, the results are plotted in terms of the pressure drop and

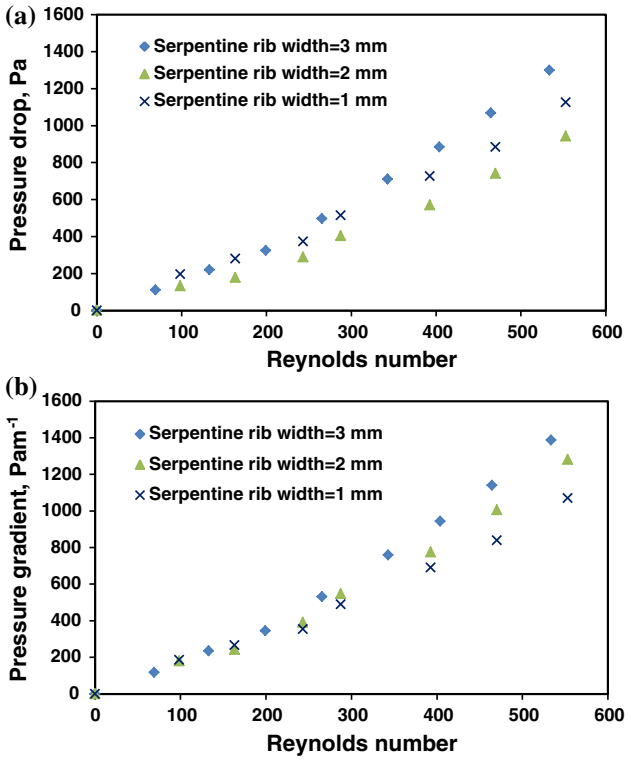

Fig. 3 Comparison of various rib widths of serpentine flow field in terms of **a** Pressure drop, **b** Pressure gradient

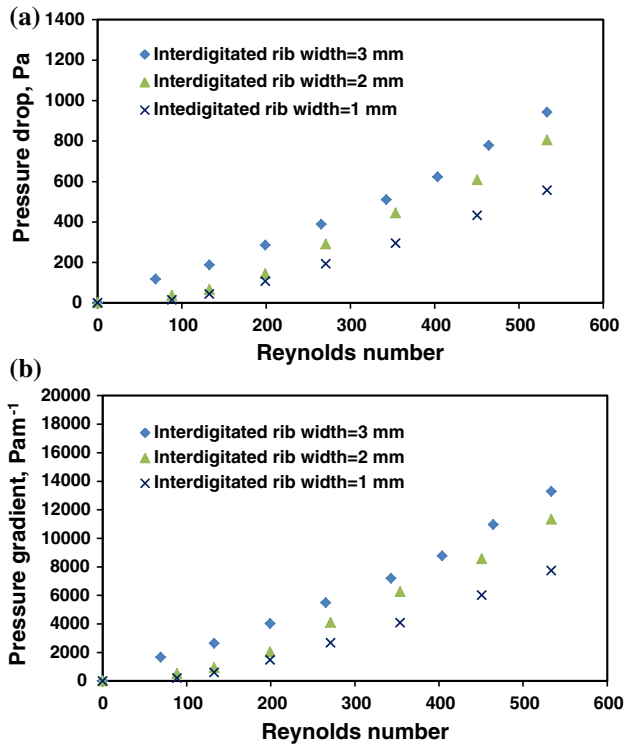

Fig. 4 Comparison of various rib widths of interdigitated flow field in terms of **a** Pressure drop, **b** Pressure gradient

pressure gradient. It can be seen that there is a significant effect of rib width on the pressure drop for both the flow fields. The effect is one of decreasing pressure drop with decreasing rib width. While it appears that the pressure drop with 1 mm rib width is higher than that for 2 mm rib width (Fig. 3a) for the serpentine flow field, the difference is due to the difference in traversed length. The corresponding pressure gradients (Fig. 3b) show that decreasing rib width reduces the pressure gradient, the difference being about 30 % when the rib width is reduced from 3 to 1 mm. For the interdigitated flow field, the effect is even stronger and amounts to about 45 %. One may note from Figs. 3 and 4 that while the pressure drop between the inlet and the outlet of the cell is less for the interdigitated flow field, the pressure gradient is much higher reflecting the fact that flow is going through a porous medium with a considerably smaller effective diameter than the flow in the channel. The reduction in the overall pressure drop can be attributed to the lesser volumetric flow rate through each parallel channel and to the shorter traverse length in case of the interdigitated flow field.

3 CFD analysis of the serpentine and interdigitated flow fields

For more insight into the hydrodynamics of these flow fields, CFD analysis, similar to that reported in [20], has been carried out. The computational domain for flow consisted of the flow field and the porous substrate (see Fig. 1). The serpentine or interdigitated flow field was created by hewing out the flow volume from an originally flat plate of constant thickness. A porous volume representing the liquid diffusion layer (carbon felt) of appropriate dimensions was placed below it; the common face between the two volumes was treated as an internal surface which offered no resistance to fluid flow. The inlet and the outlet of the channel were located at opposite ends. While the reactant flows through this non-porous serpentine channel, it reaches surface of the porous medium and forms a way through it by diffusion and convection. Experimentally determined permeability values of compressed and uncompressed carbon felt are specified in the porous medium under the rib and under the flow channel, respectively. A specified uniform flow velocity at the inlet, zero gage pressure at the outlet, and the no-slip condition on the walls were the imposed boundary conditions on the flow domain. All the simulations were carried out using Fluent 6.3.26. Second-order accuracy was maintained in the discretization for all the terms. Grid independence test was carried out using four grids with a total number of 1.51×10^5, 7.02×10^5, 12.11×10^5, and 23.11×10^5 cells. It was observed that except in the case of the smallest

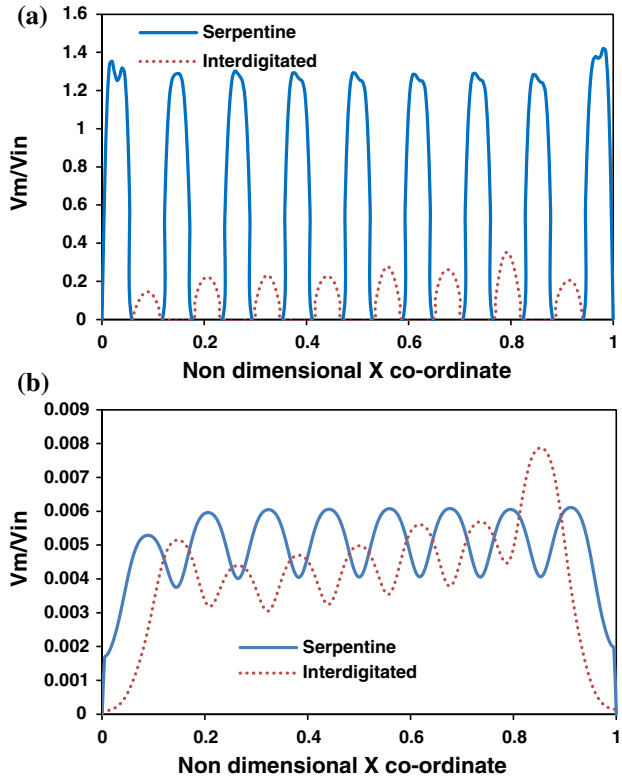

Fig. 5 Comparison of velocities at **a** mid channel height, **b** mid electrode height using serpentine and interdigitated flow fields Vin = 0.201 ms^{-1} (80 × 51 mm; rib width = 3 mm), K = 7.5 × 10^{-11} m^2

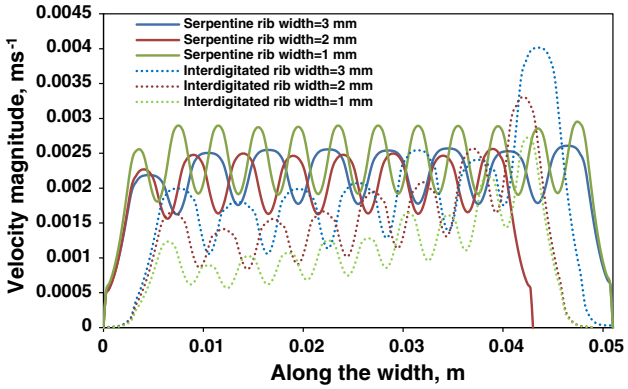

Fig. 6 Effect of rib width on the flow velocity in the porous carbon felt region

number of cells (1.5 × 10^5), the solution obtained with the other three grids was nearly the same. In view of this, the grid spacing in the simulation with 12.11 × 10^5 cells was used as a guideline figure in further calculations.

In the simulations, the full geometrical details (i.e., all the bends and straight sections) of the top plate containing the flow field were considered. The carbon felt was treated as a porous medium with a specified permeability of 7.5 × 10^{-11} m^2 when uncompressed and 4.5 × 10^{-11} m^2 when compressed [20]. The inlet and the outlet were modeled as per the geometry of the experiments. The flow field was calculated using fairly routine CFD practice. The primary interest in these calculations was to determine the nature and extent of convection in the carbon felt. The predicted velocities at mid-height of the channel and mid-height of the carbon felt are shown in non-dimensional quantities in Fig. 5a and b, respectively, for an inlet velocity of 0.201 ms^{-1}, which corresponds to a Reynolds number of 600. It can be seen from Fig. 5a that in the serpentine flow field, most of the flow goes through the channel and is fairly uniform in all the channels, which is to be expected in this flow field. The velocity in the interdigitated flow field is considerably less as the total flow rate is divided among several flow channels. The distribution among the parallel (inlet or outlet) channels is not as uniform as in the serpentine flow field; however, it is fairly uniform. The flow velocity through carbon felt (Fig. 5b) is surprisingly less for the interdigitated flow field (IFF) than for the serpentine flow field (SFF). Since all the flow through the channels would have to go through the carbon felt in the IFFs, one would have expected significantly higher velocity in the IFF than in the SFF. However, this stands to reason when one considers the fact that the flow rate through the individual channels of IFF is considerably less than that through the serpentine channel (see Fig. 5a).

The effect of rib width on the flow velocity in the carbon felt, which is important from the perspective of mass transfer over potential for the electrochemical reaction that is occurring in the porous region, is shown in Fig. 6. Here, the computed variation along the width of the active region of the 80-mm-long cell is shown for rib widths of 1, 2, and 3 mm for the IFF and the SFF. It may be noted that the width is about 51 mm for the 1 mm and the 3 mm rib widths in the SFF while it is less by about 15 % in the 2 mm rib width case. As expected, the rib width has only a small effect on the mid-felt velocity in the SFF with a small increase, when the rib width is decreased. A similar effect is seen in the case of the IFF; however, there is a significant maldistribution of the velocity along the width and this maldistribution becomes more pronounced, when the rib is decreased.

Thus, prima facie, it appears that the IFF would fare poorly from an electrochemical cell performance point of view in comparison with the SFF. Although the pressure drop is considerably lower for the same inlet flow rate, the convective velocity of the reactant in the carbon felt is lower by to 30–50 % compared to the SFF at the same flow rate of the reactant through a cell of the same active area. In addition, the flow distribution is less uniform. However, studies [34] show that the electrochemical performance of

the IFF is actually better than that of SFF. In order to resolve this contradiction, further analysis of the flow fields predicted by CFD has been carried out. In order to bring out the characteristics of the cross-flow, the predicted path lines (of mass less particles which would follow the fluid) have been analyzed for the same overall flow rates and the same overall dimensions of the cell. Figure 7 shows the predicted path lines, colored by the residence time, of the mass less fluid particles are shown for the two flow fields. For clarity, both the front view and the back view of the path lines are shown. It can be seen that there is extensive and widely distributed flow circulation in the carbon felt both cases. However, the path lines in the IFF have very low residence times whereas those in the SFF have a much larger residence time. There is a tendency in the SFF case for an undercurrent of the cross-flow to exist all the way from the first (inlet) segment to the last (outlet) segment. This is reflected in the long residence times of these path lines. In the IFF, the path lines are mostly blue in color indicating a short residence time. This is because most of the flow enters the porous medium from one inlet channel, traverses a short distance in the carbon felt, and then re-enters the adjacent outlet channels, thus giving a much lower residence time. Since the electrochemical reactions are occurring all along the flow path in the porous medium at more or less the same rate, the reactant concentration decreases further and further as it spends more and more time in the reactor. Thus, a short residence time (as in the IFF) implies a fresh reactant, while a long residence time (as in the SFF) would imply more dilute reactant and worse electrochemical performance. Thus, the residence time plots shown in Fig. 7 are consistent with the increased effectiveness of the IFF in feeding fresh reactant to the carbon felt.

In order to confirm this experimentally, a limited number of experiments were conducted in a single-cell VRFB of the single all-vanadium redox flow (VRB) cell of active area 40.8 cm^2 using 2 M 99.9 % $VOSO_4 \cdot xH_2O$ (Alfa Aesar) in 2 M sulfuric acid solution as the electrolyte. Two layers of carbon felt, each of thickness 3 mm and compressed by 20 % in thickness, were used as electrode on each side and were separated by Nafion 117 membrane (Sigma Aldrich). The electrochemical performance of VRFB cell with serpentine and interdigitated flow fields was analyzed using polarization curves. These are shown in Fig. 8; although the results appear to be contaminated by large cell resistance, one can see that both the polarization curve and the power density curve showed improved performance with the interdigitated flow field. Further testing, over a wide range of geometrical and flow conditions, is necessary to obtain a clear indication. The present study brings out a qualitative difference in the circulation pattern of the electrolyte with the serpentine and the interdigitated flow fields.

4 Segmented network model for interdigitated flow field

For system-level performance studies, it is necessary to determine the power loss required for pumping of the reactants [22]. While experimental studies of interdigitated flow fields have been conducted, no quantitative predictive models are available for RFB applications. It is possible to get an estimate using CFD studies; however, these will require significant computational effort and cannot be readily embedded in an optimization study. In previous work by one of the present authors [38], a hydrodynamic network model for IFF for fuel cell applications was proposed. In this model, the flow rate along the length of the inlet or outlet channel was assumed to be uniform. For a flow battery application, the permeability of the electrode and its thickness are almost one magnitude higher than that of the fuel cell. Thus, the uniform variation may not necessarily hold good in this case. Therefore, a segmented network model, shown schematically in Fig. 9, has been developed for flow battery applications. Here, the inlet and the outlet headers as well as the inlet and the outlet channels are divided into short segments, which, when put together, will represent the entire flow field. Each segment includes a channel section and the underlying porous medium (carbon felt). The flow of the electrolyte between adjacent segments can occur through directly connected channel segments and also via cross-flow through the porous medium. Each segment and flow path offer a flow resistance which is characteristic of the geometric and permeability characteristics (if applicable) of the flow path. Following the electrical analogy among voltage, current, and electrical resistance, one can conceptualize a hydrodynamic analogy among pressure, flow rate, and flow resistance. The relation among these variables is simpler in electrical circuits; in fluid flow, non-linear effects (for example, those associated with pressure recovery, two-phase flow [38]) may be present. Assuming linear relationship between pressure drop and flow rate (which is applicable for fully developed laminar flow through ducts and porous media), the following frictional resistance terms can be written for each segment in terms of the geometric and dynamic parameters of the flow [38]:

For inlet and outlet channels,

$$R_c = \frac{(\mathrm{Ref})_c \mu P_c L_c}{2\rho D_c A_c^2}. \quad (1)$$

Here, ρ and μ are the density and the dynamic viscosity of the fluid; D_c, P_c, L_c, and A_c are the hydraulic diameter, the wetted perimeter, the length, and the cross-sectional area of the channel segment, respectively. $(\mathrm{Ref})_c$ is given by an empirical correlation of Kays and Crawford [40]:

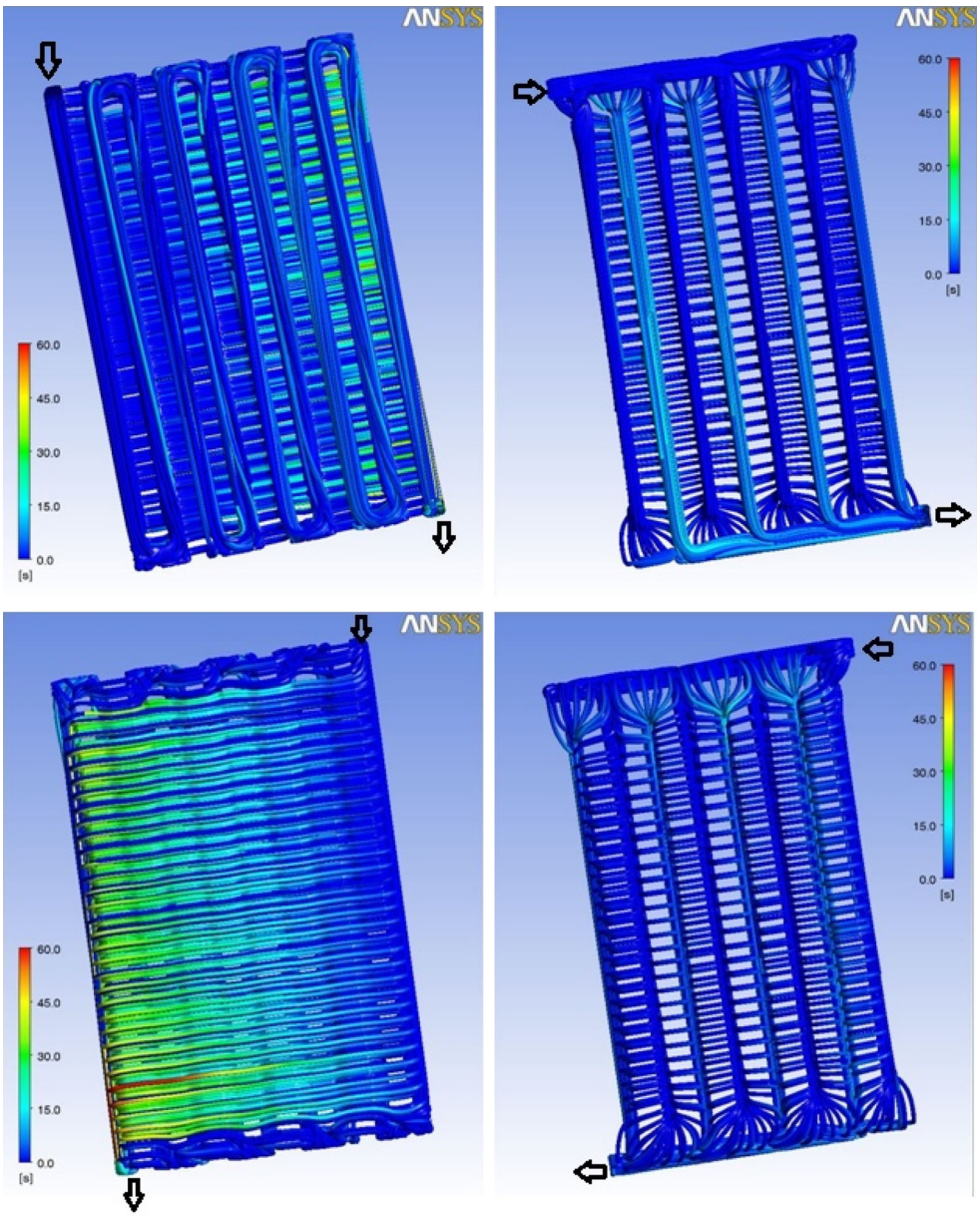

Fig. 7 Numerically simulated path lines of serpentine and interdigitated flow fields; *front* view and *back* view (Vin = 0.226 ms^{-1})

$$(\mathrm{Ref})_c = 13.84 + 10.38 \exp\left(-\frac{3.4}{a}\right), \tag{2}$$

where 'a' is the channel aspect ratio (width/depth). For flow resistance through porous medium,

$$R_g = \frac{\mu W_{rc}}{K \rho A_g}, \tag{3}$$

$A_g = L_c \times t_g$ is the cross-sectional area of the rib, t_g is thickness of the porous layer, and K is the permeability of the porous medium and

$$W_{rc} = W_r + f.\left(t_g + \frac{W_c}{2}\right) \tag{4}$$

is the effective rib width or the traverse length through the porous medium. This is arrived at as follows. As shown schematically in Fig. 9b, in order to enter the outlet channel from the inlet channel, the fluid has to flow down a distance of $t_g/2$ before it reaches the mid-height of the carbon felt under the channel, followed by a distance of $W_c/4$ (since the inlet channel feeds to two neighboring outlet channels) before it reaches the portion under the rib, followed by a distance of rib width W_r to come under the outlet channel, followed by a distance of $W_c/4$ and a further height of $t_g/2$. This path is an idealized path and in the actual case, there can be some short-circuiting of the path in the portion under the channels; this effect is considered through the factor f which lies between 0 and 1.

All the inlet channels and outlet channels are connected to a common inlet and outlet header. The total header resistance in any segment consists of frictional resistance and accelerational pressure drop component arising out of flow rate changes. Following [38], these are evaluated as follows:

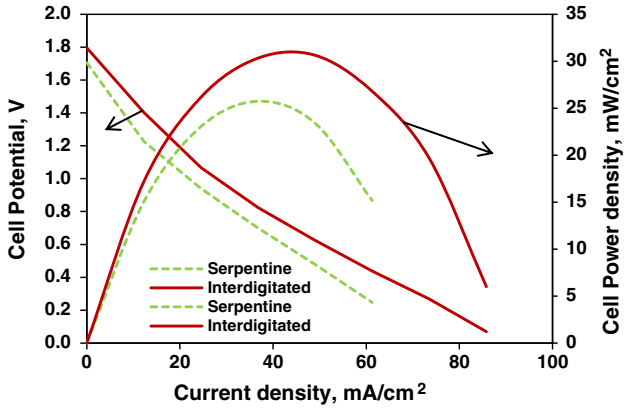

Fig. 8 Measured polarization performance of a single-cell VRFB with serpentine and interdigitated flow fields

$$R_{\mathrm{h}} = \frac{(\mathrm{Ref})_{\mathrm{h}}\mu(P_{\mathrm{h}}L_{\mathrm{h}} + A_{\mathrm{t}})}{2\rho D_{\mathrm{h}}A_{\mathrm{h}}^2} + P_{\mathrm{acc},k}, \tag{5}$$

where $P_{\mathrm{acc,k}}$ is the accelerational pressure drop component in the kth segment. For an inlet header segment between k and $k + 1$, this term is evaluated as

$$P_{\mathrm{acc,k}} = P_{\mathrm{acci,k}} = \frac{m_{\mathrm{hi},k} - \frac{m_{\mathrm{hi,k-1}}^2}{m_{\mathrm{hi,k}}}}{2\rho A_{\mathrm{h}}^2}. \tag{6}$$

The term for the outlet header segment between k and $k + 1$ outlet channels is as follows:

$$P_{\mathrm{acc},k} = P_{\mathrm{acco},k} = \frac{m_{\mathrm{ho},k} - \frac{m_{\mathrm{ho},k-1}^2}{m_{ho,k}}}{2\rho A_{\mathrm{h}}^2}. \tag{7}$$

Here, P_{h}, L_{h}, and A_{h} are respectively the wetted perimeter, the length, and the cross-sectional area of the header segment, and m_{hi}, m_{ho} are the mass flowrates in the ith inlet and outlet header segments. Since these terms are unknown a priori, the evaluation of the accelerational component of the flow resistance is done iteratively [38].

The implementation of the segmented interdigitated flow field model is relatively straightforward. The IFF is divided into equal number of segments along the length of

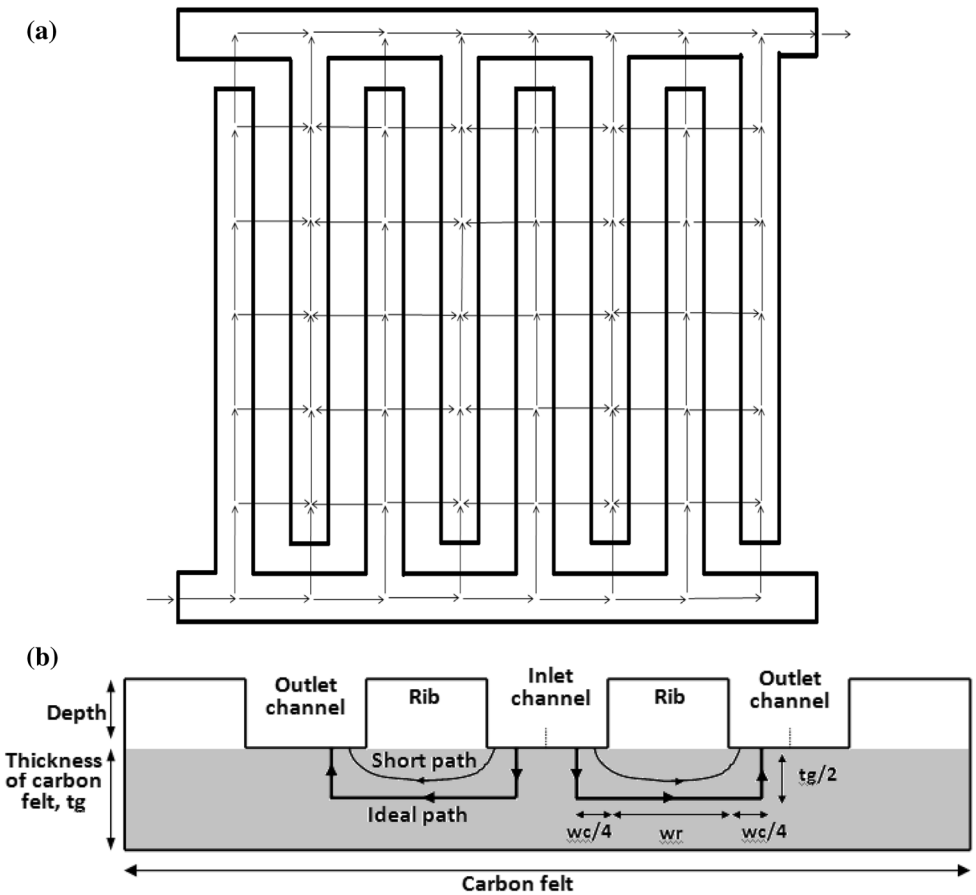

Fig. 9 Schematic representation of **a** segmented interdigitated flow field **b** transverse length through the porous medium

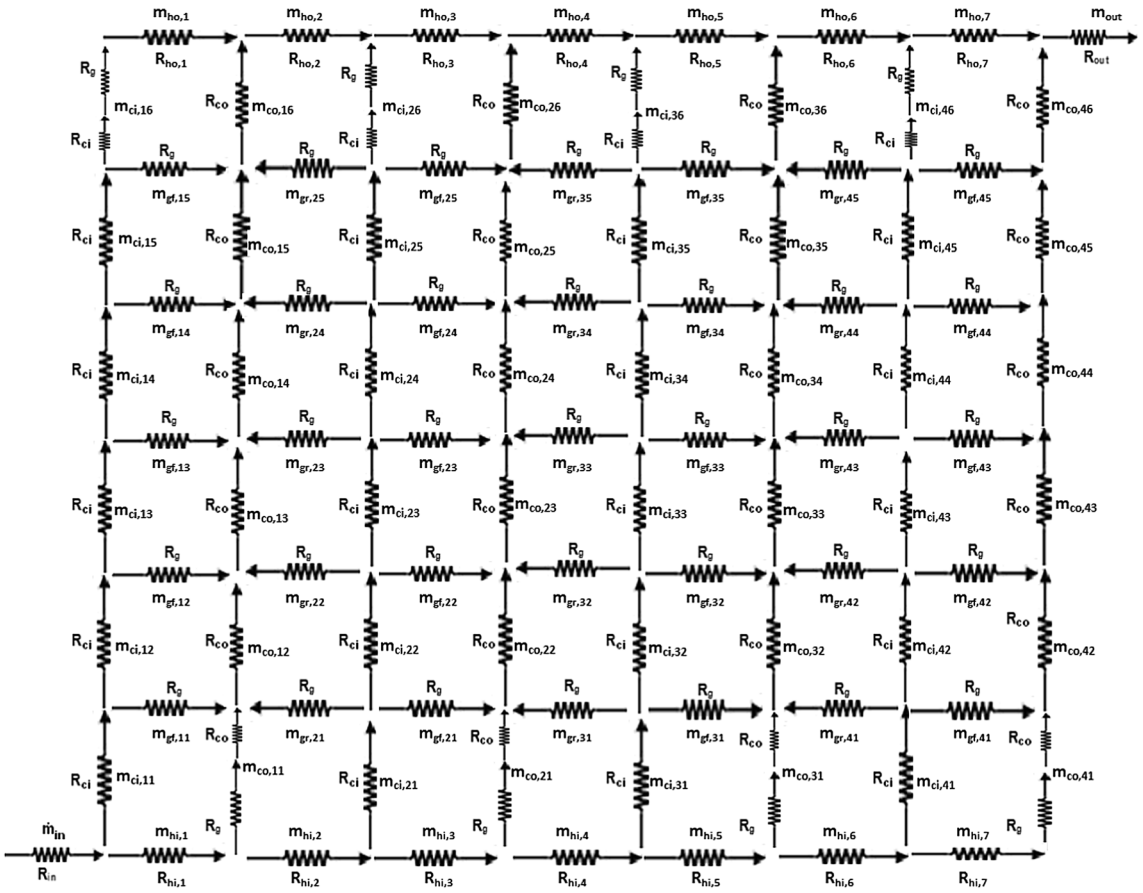

Fig. 10 Segmented hydrodynamic network diagram for a 4-pair interdigitated flow field

the straight channel. Each segment is associated with the flow resistance in the channel and porous medium under the rib. The interconnection of these resistances in a single segment forms a closed loop analogous to an electrical circuit. Flow through an inlet and outlet channel pair is represented as a combination of these loops/circuits and forms a network diagram. The network diagram for an interdigitated flow field with four-inlet and a four- outlet channel IFF segmented into six channel segments and seven header segments (Fig. 9a) resulting in 42 loops is shown in Fig. 10. Applying Kirchhoff's voltage law, which states that the algebraic sum of the voltages around any closed path in a circuit is zero, for each loop in the network diagram, a system of algebraic equations in terms of unknown mass flow rates is obtained. These set of equations are ordered in a matrix form as RM = B with R as the resistance matrix, M as the unknown mass flow rates in the segments, and B as the constant matrix. The obtained mass flow rates are used to calculate the flow rates in outlet channels. The total pressure drop is determined using the resistances and corresponding mass flow rates in the channel segments.

A 42-loop segmented model has been developed for the IFFs used in the present experimental study. The predicted pressure drops using the segmented hydrodynamic network model (HNM) is plotted as a function of Reynolds number and compared with the predictions from CFD simulations and the experimental data in Fig. 11, separately for each rib width. As mentioned in a previous study [20], the carbon felt is subject to significant compression and this effectively reduces the depth of the channels in the flow field. Using CFD simulations and the present experimental data, this has been estimated to be 48, 44, and 38 % for 3, 2, and 1 mm rib width cases. The same values have been used to compute the effective channel depth in the HNM study. The experimentally determined value [20] of 4.5×10^{-11} m^2 for the permeability of the compressed electrode is used in HNM calculations. The value of f in Eq. (4), which determines the effective traverse path through the porous medium, is taken to be 0.1 while calculating resistance through the porous medium. It can be seen from Fig. 11 that the HNM model predicts the experimental data well over the entire range of Reynolds number and that the agreement is equally good for the three rib widths considered in the study. The

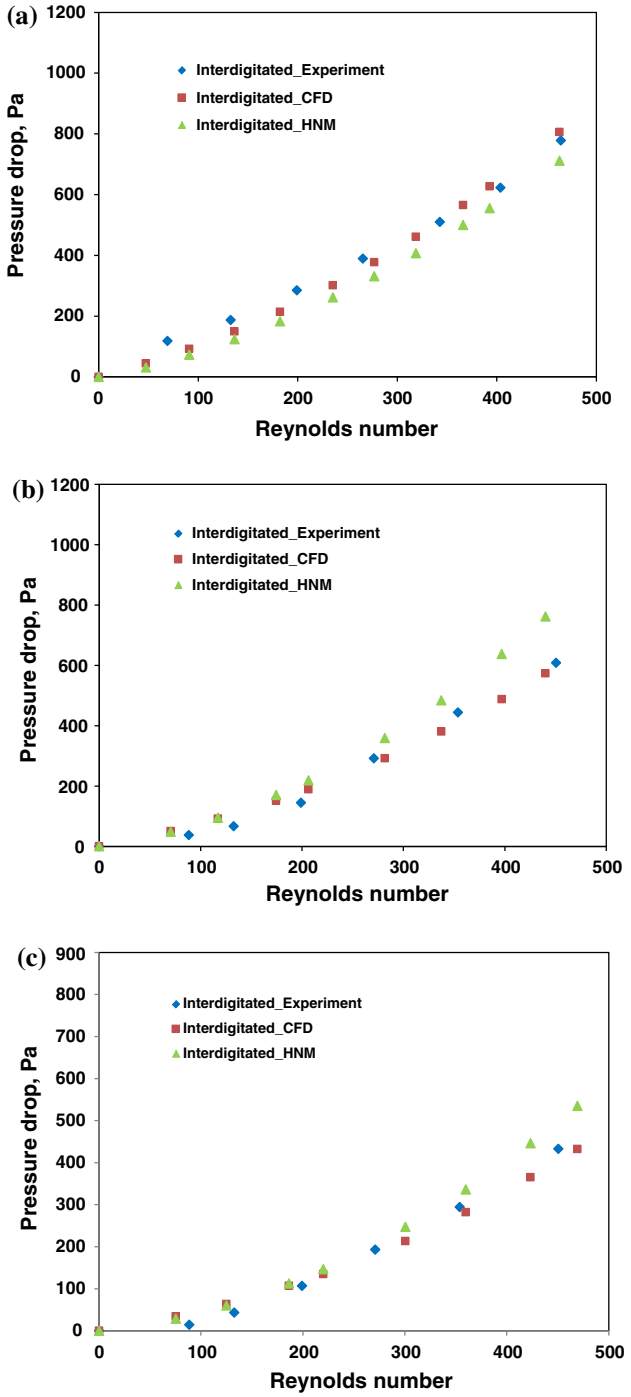

Fig. 11 Comparison between CFD simulations, HNM and experimental data of 80 × 51 mm using **a** 3 mm **b** 2 mm **c** 1 mm rib widths for an interdigitated flow plate

computational time for the HNM is of the order of a few seconds and it thus gives an acceleration of three orders of magnitude over CFD simulation for the corresponding case. It can therefore be readily used in system level simulations of RFB energy storage units.

5 Conclusions

The overall VRFB system efficiency can be increased by minimizing parasitic energy loss. The contribution of pumping power to this can be determined using pressure drop characteristics. The present work reports a detailed study on one of the important factors, namely, flow field design, that contribute markedly to the overall pressure drop and the electrochemical performance. The pressure drop and flow distribution characteristics of two widely used flow fields have been studied experimentally and theoretically. The following conclusions can be drawn from the present study:

- The pressure drop required for the circulation of the electrolyte is a significant parasitic power loss component that appears in the calculation of the round-trip efficiency. The present experimental results show that for typical VRFB applications, the pressure drop in an interdigitated flow field is less than that for a serpentine flow field. A calculation methodology for the estimation of pressure drop in an interdigitated flow field of other dimensions is proposed.
- The present study also underscores the idea that pressure drop alone is not the important criterion, when flow fields such as serpentine and interdigitated are used. The transport of the reactants to the reaction zone is also very important. The present results show that the same cell size and for the same electrolyte flow rate, the under-the-rib convection in a serpentine flow field is as strong as it is in interdigitated flow fields.
- The present study also brings out the qualitative difference in the under-the-rib convection of the electrolyte brought about by the two flow fields. The reported better electrochemical performance of the interdigitated flow field, which is also confirmed through limited testing reported in the present study, has been interpreted in terms of the residence time of the electrolyte in the reaction zone. More studies have to be conducted about this over a wider range of flow and geometric conditions; possibility thus exists for optimization of the flow field for best overall round-trip efficiency of the cell.

References

1. Horne CR, Mosso RJ (2013) Introducing EnerVault's engineered cascade system: results from a novel redox flow battery architecture and use of mixed-species iron chromium electrolytes. Int Flow Battery Forum Proc 24–25
2. Weber AZ, Mench MM, Meyers JP, Ross PN, Gostick JT, Liu Q (2011) Redox flow batteries: a review. J Appl Electrochem 41:1137–1164. doi:10.1007/s10800-011-0348-2

3. Yang Z, Liu J, Baskaran S, Imhoff CH, Holladay JD (2010) Enabling renewable energy- and the future grid-with advanced electricity storage. JOM 62:14–23
4. Yang Z, Zhang J, Kinter-Meyer MCW, Lu X, Choi D, Lemmon JP, Liu J (2011) Electrochemical energy storage for green grid. Chem Rev 111:3577–3613
5. Skyllas-Kazacos M (2013) Flow battery research to flow battery commercialization. Int Flow Battery Forum Proc 42–44
6. Li L, Kim S, Wang W, Vijayakumar M, Nie Z, Chen B, Zhang J, Xia G, Hu J, Graff G, Liu J, Yang Z (2011) A stable vanadium redox-flow battery with high energy density for large-scale energy storage. Adv Energy Mater 1:394–400. doi:10.1002/aenm.201100008
7. Sun B, Skyllas-Kazacos M (1992) Modification of graphite electrode materials for vanadium redox flow battery application-I. Therm treat Electrochim Acta 37:1253. doi:10.1016/0013-4686(92)85064-R
8. Sun B, Skyllas-Kazacos M (1992) Chemical modification of graphite electrode materials for vanadium redox flow battery application-part II. Acid Treat Electrochim Acta 37:2459. doi:10.1016/0013-4686(92)85064-R
9. Pittman CU Jr, Jiang W, Yue ZR, Gardner S, Wang L, Toghiaiband H, Leon CAL (1999) Surface properties of electrochemically oxidized carbon fibers. Carbon 37:1797–1807. doi:10.1016/S0008-6223(99)00048-2
10. Sun BT, Skyllas-kazacos M (1991) Chemical modification and electrochemical behaviour of graphite fibre in acidic vanadium solution. Electrochim Acta 36:513–517. doi:10.1016/0013-4686(91)85135-T
11. Wang W, Luo Q, Li B, Wei X, Li L, Yang Z (2013) Recent progress in redox flow battery research and development. Adv Funct Mater 23:970–986. doi:10.1002/adfm.201200694
12. Li B, Gu M, Nie Z, Shao Y, Luo Q, Wei X, Li X, Xiao J, Wang C, Sprenkle V, Wang W (2013) Bismuth nanoparticle decorating graphite felt as a high-performance electrode for an all-vanadium redox flow battery. Nano Lett 13:1330–1335. doi:10.1021/nl400223v
13. Kim S, Thomsen E, Xia G, Nie Z et al (2013) 1 kW/1 kWh advanced vanadium redox flow battery utilizing mixed acid electrolytes. J Power Sources 237:300–309. doi:10.1016/j.jpowsour.2013.02.045
14. Li B, Li L, Wang W, Nie Z, Chen B, Wei X, Luo Q, Yang Z, Sprenkle V (2013) Fe/V redox flow battery electrolyte investigation and optimization. J Power Sources 229:1–5
15. Wei X, Nie Z, Luo Q, Li B, Sprenkle V, Wang W (2013) Polyvinyl chloride/silica nanoporous composite separator for all-vanadium redox flow battery applications. J Electrochem Soc 160:A1215–A1218. doi:10.1149/2.087308jes
16. Wei X, Nie Z, Luo Q, Li B, Chen B, Simmons K, Sprenkle V, Wang W (2013) Nanoporous polytetrafluoroethylene/silica composite separator as a high-performance all-vanadium redox flow battery membrane. Adv Energy Mater 3:1215–1220. doi:10.1002/aenm.201201112
17. Hoberecht MA (1981) Pumping power considerations in the designs of NASA-Redox flow cells. US DOE Report No. DOE/NASA/12726-7 NASA TM-82598
18. Li X, Sabir I (2005) Review of bipolar plates in PEM fuel cells: Flow-field designs. Int J Hydrog Energy 30:359–371. doi:10.1016/j.ijhydene.2004.09.019
19. Suresh PV, Jayanti S, Deshpande AP (2011) An improved serpentine flow field with enhanced cross-flow for fuel cell applications. Int J Hydrog Energy 36:6067–6072. doi:10.1016/j.ijhydene.2011.01.147
20. Jyothi Latha T, Jayanti S (2014) Ex-situ experimental studies on serpentine flow field design for redox flow battery systems. J Power Sources 248:140–146. doi:10.1016/j.jpowsour.2013.09.084
21. Shyam Prasad KB, Jayanti S (2008) Effect of channel-to-channel cross-flow on local flooding in serpentine flow-fields. J Power Sources 180:227–231. doi:10.1016/j.jpowsour.2008.01.074
22. Xiong B, Zhao J, Tseng KJ, Skyllas-Kazacos M, Lim TM, Zhang Y (2013) Thermal hydraulic behavior and efficiency analysis of an all-vanadium redox flow battery. J Power Sources 242:314–324. doi:10.1016/j.jpowsour.2013.05.092
23. Kee JR, Korada P, Walters K, Pavol M (2002) A generalized model of the flow distribution in channel networks of planar fuel cells. J Power Sources 109:148–159. doi:10.1016/S0378-7753(02)00090-3
24. Maharudrayya S, Jayanti S, Deshpande AP (2005) Flow distribution and pressure drop in parallel-channel configurations of planar fuel cells. J Power Sources 144:94–106. doi:10.1016/j.jpowsour.2004.12.018
25. Miyabayashim M, Sato K, Tayama T, Kageyama Y, Oyama H (1998) Redox Flow type battery. US Patent 5,851,694
26. Inoue M, Kobayashi M (1997) Electrode material for flow through type electrolytic cell, where in the electrode comprises carbonaceous material having at least one groove. US Patent 5,648,184
27. Harper MAM (2010) Electrochemical battery incorporating internal manifolds. US Patent 7,682,728
28. Harper MAM (2010) Electrochemical battery incorporating internal manifolds. US Patent 7,687,193
29. Tiana C-H, Cheina R, Hsueh K-L, Wu C-H, Tsau F-H (2011) Design and modeling of electrolyte pumping power reduction in redox flow cells. Rare Met 30:16. doi:10.1007/s12598-011-0229-1
30. Chen J-Q, Wang B-G, Yang J-C (2009) Adsorption and diffusion of VO^{2+} and VO_2^{+} across cation membrane for all-vanadium redox flow battery. Solvent Extr Ion Exch 27:312–327. doi:10.1080/07366290802674614
31. Xu Q, Zhao TS, Leung PK (2013) Numerical investigations of flow field designs for vanadium redox flow batteries. Appl Energy 105:47–56. doi:10.1016/j.apenergy.2012.12.041
32. Zhu SQ, Chen JQ, Wang Q, Wang BG (2008) Influence of flow channel structure and electrolyte flow state on the performance of VRB. Battery 38:285–287
33. Aaron DS, Liu Q, Tang Z, Grim GM, Papandrew AB, Turhan A, Zawodzinski TA, Mench MM (2012) Dramatic performance gains in vanadium redox flow batteries through modified cell architecture. J Power Sources 206:50–453
34. Tsushima S, Sasaki S, Hirai S (2013) Influence of cell geometry and operating parameters on performance of a redox flow battery with serpentine and interdigitated flow fields. In: Proceedings of ECS Meeting, San Francisco, October, 1664
35. Koeppel BJ, Recknagle K, Stephenson D, Reed D, Thomsen Ed, Sprenkle V (2013) Redesign of a vanadium redox flow battery for reduced pressure loss using an interdigitated flow field. In: Proceedings of ECS Meeting, San Francisco, October, 1660
36. Qiu G, Joshi AS, Dennison CR, Knehr KW, Kumbur EC, Sun Y (2012) A 3-D pore-scale resolved model for coupled species/charge/fluid transport in a vanadium redox flow battery. Electrochim Acta 64:46–64
37. Escudero-González J, López-Jiménez PA (2014) Methodology to optimize fluid-dynamic design in a redox cell. J Power Sources 251:243–253
38. Shyam Prasad KB, Suresh PV, Jayanti S (2009) A hydrodynamic network model for interdigitated flow fields. Int J Hydrog Energy 34:8289–8301. doi:10.1016/j.ijhydene.2009.07.107
39. Hsieh SS, Yang SH, Kuo JK, Huang CF, Tsai HH (2006) Study of operational parameters on the performance of micro PEMFCs with different flow fields. Energy Convers Manag 47:1868–1878. doi:10.1016/j.enconman.2005.10.011
40. Kays WM, Crawford ME (1980) Convective heat and mass transfer. Mc Graw-Hill, New York